1   # Structural studies reveal that endosomal cations promote formation of
2   infectious CVA9 A particles, facilitating RNA and VP4 release.

3

4   Aušra Domanska[1,3], Zlatka Plavec[1,3], Visa Ruokolainen[2,3], Benita Löflund[1], Varpu Marjomäki[2], Sarah

5   J Butcher[1,4],

6   [1]Faculty of Biological and Environmental Sciences, Molecular and Integrative Bioscience Research

7   Programme, and Helsinki Institute of Life Sciences-Institute of Biotechnology, University of

8   Helsinki, Helsinki, Finland

9   [2]Department of Biological and Environmental Sciences, Nanoscience Center, University of Jyväskylä,

10   Finland

11   [3]Equal contribution

12   [4]Corresponding Author

13   **Running title:** Ions and albumin expanding CVA9 structure

14   emails in order: ausra.domanska@helsinki.fi, zlatka.plavec@helsinki.fi, visa.ruokolainen@jyu.fi,

15   benita.loflund@helsinki.fi, varpu.s.marjomaki@jyu.fi, sarah.butcher@helsinki.fi

16

Abstract

Coxsackievirus A9, an enterovirus, is a common cause of paediatric aseptic meningitis and neonatal sepsis. During cell entry, enterovirus capsids undergo conformational changes leading to expansion, formation of large pores, externalization of VP1 N-termini and loss of the lipid factor from VP1. Factors such as receptor binding, heat, and acidic pH can trigger capsid expansion in some enteroviruses. Here we show that fatty-acid free bovine serum albumin or neutral endosomal ionic conditions can independently prime CVA9 for expansion and genome release. Our results show that CVA9 treatment with albumin or endosomal ions generates a heterogeneous population of virions, which could be physically separated by asymmetric flow field flow fractionation and computationally by cryo-EM and image processing. We report cryo-EM structures of CVA9 A-particles obtained by albumin or endosomal ion treatment and a control non-expanded virion to 3.5, 3.3 and 2.9 Å resolutions, respectively. Where albumin promotes stable expanded virions, the endosomal ionic concentrations induce unstable CVA9 virions which easily disintegrate losing their genome. Loss of most of the VP4 molecules and exposure of negatively-charged amino acid residues in the capsid's interior after expansion, create a repulsive viral RNA-capsid interface, aiding genome release.

Importance

Coxsackievirus A9 (CVA9) is a common cause of meningitis and neonatal sepsis. The triggers and mode of action of RNA release into the cell unusually do not require receptor interaction. Rather, a slow process in the endosome, independent of low pH is required. Here, we show by biophysical separation, cryogenic electron microscopy and image reconstruction that albumin and buffers mimicking the endosomal ion composition can separately and together expand and prime CVA9 for uncoating. Furthermore, we show in these expanded particles that VP4 is present at only ~10% of the occupancy found in the virion, VP1 is externalised and the genome is repelled by the negatively-charged, repulsive inner surface of the capsid that occurs due to the expansion. Thus, we can now link observations from cell biology of infection with the physical processes that occur in the capsid to promote genome uncoating.

Introduction

Coxsackievirus A9 (CVA9) belongs to the *Enterovirus* genus, *Enterovirus B* species (EV-B) in the family *Picornaviridae*. CVA9 can frequently cause paediatric aseptic meningitis and neonatal sepsis (1-4). Like other picornaviruses, CVA9 has a small, ~30 nm in diameter, non-enveloped viral capsid. Its (+)ssRNA genome is ~7 500 bases long and encodes for 4 structural (VP1-4) and 7 non-structural proteins (2A-C, 3A-D) (5). Expanded A-particles are described for many enteroviruses, occurring at early steps during virus entry (6-10). It is thought that VP4 must be present in the A-particle to be infectious, but VP4 is very difficult to detect (11). Many picornaviruses, including members of the EV-B, accommodate a lipid factor in the VP1 hydrophobic pocket. Palmitate is a commonly found lipid factor/fatty acid in enteroviruses (12). Expulsion of the lipid factor is associated with virion expansion. Once expansion has occurred, and the capsid has been endocytosed, genome release can occur (13). It has been shown that receptor binding can trigger a loss of the lipid factor and virion expansion in some of the EV-B members (14), but not in CVA9 and echovirus 1 (E1) (15-17). In addition, CVA9 and E1 do not depend on low pH for genome release, unlike members of *Enterovirus A* species indicating that these viruses use additional cues for uncoating (15, 18). Despite extensive research, the physiological triggers leading to enterovirus uncoating after internalization, other than receptor binding and low pH in the endosomes, are poorly understood (19). Some reports show serum albumin as an uncoating cue for E1, E12 and coxsackievirus B3 (6, 20, 21).

It is well established that acidification is key to endosome maturation. In addition to proton influx during endosome maturation, the concentrations of other ions in the endosomal lumen such as sodium, potassium and calcium also change over time due to ion channels and pumps present in the endosomal membranes (22, 23). The absolute values of ion concentrations within the endosome structures are not known, and they can notably vary even within specific microenvironments of the endosome (22, 23). However, the general trend is a decrease in sodium and calcium concentrations and an increase in potassium concentration during the endosome maturation (24-26). Thus, changes in ion concentrations other than protons may well serve as a trigger for virus uncoating.

We showed previously that, at 37 °C, albumin in combination with a neutral buffer mimicking the endosomal environment triggers the expansion of E1 without receptor engagement creating an infectious A-particle (6). However, we did not show the individual effect of either albumin or ion changes to the overall conformational changes identified. Here we show by real-time spectroscopy, gradient ultracentrifugation, cryo-EM and image reconstruction that endosomal ionic concentrations alone are sufficient to induce CVA9 expansion at a physiologically-relevant

79 temperature. Moreover, this treatment leads to unstable CVA9 virions which easily disintegrate

80 losing their genome. Albumin alone or in combination with endosomal ionic concentrations induces

81 CVA9 expansion. We also show that particle expansion is a dynamic process yielding a mixed

82 population of virions, as assessed by gradient ultracentrifugation and cryo-EM analysis. Using

83 asymmetric flow field flow fractionation (AF4), we were able to physically separate expanded and

84 intact particles and to confirm by mass spectrometry (MS) that expanded particles largely lack the

85 small internal capsid protein, VP4. Loss of VP4 and exposure of negatively-charged amino acid

86 residues in the capsid's interior after expansion, create a repulsive viral RNA-capsid interface, aiding

87 genome release.

88

Results

89

Faf-BSA or ions prime intact CVA9 to expanded virions

90

91 We studied factors that lead to virion expansion or uncoating by monitoring changes in the viral

92 RNA (vRNA) accessibility to the fluorescent dye SYBR Green II using real-time spectroscopy. SYBR

93 Green II interacts with free non-encapsidated RNA or it can access vRNA due to the pores in the

94 expanded capsids (6, 27). In DPBS, the virions were stable for 3 hours according to the very low

95 fluorescence readout throughout the measurement (Fig. 1A, black solid line; Table 1). Addition of

96 RNase allowed us to distinguish between the signal originating from vRNA released from dissociated

97 virions and the signal from expanded RNA-containing particles where the RNA is protected (Fig. 1A-

98 B dotted lines). For CVA9 in DPBS, the addition of RNase gave lower fluorescence values indicating

99 that either nucleic acids are present in the CVA9 preparation or vRNA is released from a small

100 percentage of the virions and is degraded by the RNase (Fig. 1A, black dotted line). Incubation of

101 CVA9 in 0.01% fatty acid free bovine serum albumin (faf-BSA) induced a fluorescence signal starting

102 at 20 min and reaching its plateau at 40 min (Fig. 1B red solid line; Table 1). Faf-BSA sequesters fatty

103 acids from the virion. Addition of RNase in a parallel measurement shows only slightly decreased

104 fluorescence readout (Fig. 1B red dotted line vs red solid line). This indicates that 0.01% faf-BSA in

105 DPBS efficiently converted CVA9 into expanded particles and only a small fraction of virions

106 dissociated releasing their vRNA (Fig. 1B).

107 The same method was applied to study the effect of estimated endosomal ionic content on CVA9

108 virion expansion (Table 1). Ion-treatment caused the fluorescence signal for vRNA to be detected

109 after 15 min, which gradually increased, reaching a plateau in 3 hours (Fig. 1B, blue solid line). The

110 addition of RNase to the ion-treatment reaction reduced the fluorescent signal by half (Fig. 1B blue

111 dotted vs blue solid line) indicating that during ion treatment a significant fraction of the CVA9

112 virions released their vRNA. Thus, incubation of CVA9 in the buffer mimicking endosomal content

113 induces virion expansion and in addition RNA release from some virions.

114 The combined treatment caused an additive effect in the fluorescence signal kinetics with expansion

115 plateauing within 15 min (Fig. 1A green lines). However, it considerably reduced RNA release from

116 the virions compared to ion treatment alone (green dotted line in Fig. 1A vs blue dotted line in Fig.

117 1B).

118

119 **Sucrose gradient analysis reveals sample heterogeneity**

120 Sucrose gradient analysis of metabolically-labelled CVA9 confirmed the results of the fluorescence

121 analysis. CVA9 treated with 0.01% faf-BSA in DPBS and separated by differential ultracentrifugation

122 shifted the peak fraction compared to the control (Fig. 1C red vs grey line). This shift indicates the

123 formation of expanded particles as their migration in the sucrose gradient is slower than that of the

124 intact particles (28). In contrast, the ion treatment of CVA9 resulted in a slightly larger shift and a

125 broader peak in the sucrose gradient (Fig. 1C blue line) as well as a larger and broader peak of empty

126 virions (fractions 8-10) in accordance with the fluorescence measurements (Fig. 1B). The

127 overlapping peaks reveal incomplete separation of the particles in the gradient.

128

129 **AF4 allows separation of expanded and intact particles**

130 AF4 has been shown to be useful in virus purification instead of ultracentrifugation (29, 30), and in

131 our experiments, AF4 allowed the physical separation of expanded particles (stabilized by faf-BSA)

132 from intact ones and thus biochemical analysis of the proteins present (Fig. 2). Importantly, if VP4

133 is released from the expanded virions, it will flow through the 10 kDa cut off AF4 membrane used

134 in this experimental setup and will not reach the fraction collector. Thus the protein composition

135 analysis of the virions separated by AF4 will directly reflect only the protein composition in the

136 particle.

137 The light scattering signal in the AF4 fractograms of the untreated CVA9 showed a clear peak

138 corresponding to particles with a radius of gyration (Rg) of 12 and 12.1 nm (two separate

139 measurements) giving geometric radii (R) of 15.5 and 15.6 nm, respectively (Fig. 2A, Table 2). The

140 tail at 70-90 min elution indicates particle heterogeneity in the sample and the peaks at the end of

141 the fractogram (90-110 min) indicate aggregation. AF4 analysis of 0.01% faf-BSA-treated CVA9

142 revealed multimodal peaks indicating a few transient states of the virions with lower diffusion

143 coefficients compared to the intact virions (Fig. 2B, C). The Rg of particles corresponding to the

144 highest peak was estimated to 12.8 nm (after 1 h treatment) and 12.6 nm (after 3 h treatment)

145 giving R of 16.5 and 16.3 nm, respectively, indicating expanded virions. The peaks for soluble protein

146 eluting at early time points (about 20 min) correspond to BSA introduced in the buffer for the

147 experiment.

148 Similarly to the real time spectroscopy measurements, ion treated-CVA9 showed slow virion

149 conversion to expanded particles, as the main peak corresponds to the intact virions with an

150 estimated Rg 12.1 nm (R of 15.6 nm) and a shoulder at elution time 65-75 min corresponding to

151 expanded virions, for which Rg measurements are unreliable due to the low signal (Fig. 2D, E). The

152 slight shift of the peak for intact virions could be explained by the changes in ion composition

153 introduced by treatment.

154 Combined treatment with both ion and 0.01% faf-BSA resulted in a clearly shifted peak with a

155 particle population of Rg 12.9 nm (R 16.7 nm) (Fig. 2F). The first shoulder of the peak eluting at 60-

156 63 min (Fig. 2F) could correspond to the main peak of the 0.01% faf-BSA treated CVA9 (Fig. 2B, C).

157 The second shoulder of the sample eluting at about 65 min could correspond to the right shoulder

158 of the CVA9 treated for 3 hours with 0.01% faf-BSA only (Fig. 2F compared with Fig. 2C). In the

159 sample with the combined treatment, as the major peak (53-77 min) has no tail and there is the

160 smallest aggregation peak, we conclude the particles are expanded and stabilized by the treatment.

161 Overall, AF4 enabled us to separate the expanded particles from the intact ones in two distinct

162 peaks, which we then used for determination of the particle's protein composition by MS.

163

164 **Mass spectrometry confirms that most of VP4 is lost in expanded virions**

165 In order to investigate if VP4 is present or absent in the expanded virions, we performed MS analysis

166 on AF4 peak fractions of the untreated CVA9 and CVA9 after combined treatment (indicated in red

167 in Fig. 2A and 2F). The MS results indicate reduced spectral counts for VP4 in the treated vs the

168 control CVA9 when compared with the total counts for the other structural proteins (Suppl. Table

169 1). In the control sample, 8.8% of the spectral counts for the structural proteins correspond to VP4

170 (13 spectra out of 134), which agrees well with the stoichiometry-based calculations from the virion

171 amino acid composition where VP4 accounts for 7.8% of the total. In the treated CVA9 sample, the

172 spectra for VP4 reach only 0.9% (5 out of 533) indicating that most of the VP4 is lost in the expanded

173 particles. Due to the fractionation in AF4, free VP4 is removed from the particle peak, thus MS

174 analysis reflects only the protein present in the particles.

Palmitate prevents particle expansion

The faf-BSA effect on CVA9 particle expansion is concentration dependent. Treating the virus with 0.01% faf-BSA, equivalent to a twenty-fold excess of faf-BSA molecules per hydrophobic pocket, we observed the efficient formation of expanded virions with only a small fraction corresponding to empty capsids as analysed by sucrose gradient differential centrifugation (Fig. 3A, red line vs. grey line; Table 1). A twenty-fold lower concentration of faf-BSA (0.0005%) equal to a 1:1 molar ratio of faf-BSA per hydrophobic pocket, had only a moderate effect on the formation of expanded CVA9 particles (Fig. 3A, orange). Furthermore, in the case of the addition of an excess amount of palmitate (in relation to faf-BSA) to saturate both the faf-BSA and the virions, the CVA9 virions were protected from expansion (Fig. 3B pink). Similar results were obtained when an excess amount of palmitate was added to CVA9 ion-treatment reaction (Fig. 3B blue vs. light blue line).

The heterogeneous particle population can be separated computationally

We used cryo-EM to analyze the intact CVA9 virions which were used as the input for faf-BSA or ion-treatment as well as the endpoint of the treatment achieved after 1 h (for faf-BSA treatment) or 3 h (for ion-treatment) at 37 °C. Multiple rounds of 2D and 3D classifications, including focused classification, revealed several different particle types in all three data sets (Fig. 4 and 5; Table 3). As expected, the main particle population in the control data set was that of intact particles (89%), but there were also expanded particles containing viral genome (5%) and empty non-expanded capsids observed (6%) (Fig. 5A). The low number of expanded and empty particles in the control data set corresponds well with the low fluorescence signal from the untreated CVA9 sample (Fig. 1A black lines); moreover, empty capsids may have released their RNA during storage which was detected in the fluorescent measurement with RNase or there was nucleic acid impurity in the sample (Fig. 1A black dashed line). In faf-BSA and ion-treated CVA9 data sets the main populations, 68% and 94.4% respectively, conform to expanded virions containing the viral genome (Fig. 5B, C). In addition, the faf-BSA-treated CVA9 data set contained a significant number of intact (non-expanded) and empty expanded particles, in agreement with the AF4 results showing a signal for intact particles in addition to expanded ones (Fig. 2B). The ion-treated CVA9 data set had the lowest percentage of intact and empty expanded particles (Fig. 5C). Free RNA detected as a drop in fluorescence signal when RNase was added (Fig. 1B blue dashed line), AF4 results showing a peak primarily for intact particles (Fig. 2D and E), and the overall low particle number picked from the micrographs (Table 3) indicate particle instability after ion treatment. In both, faf-BSA and ion-

207 treated CVA9 data sets, the empty capsids were expanded with an enlarged capsid diameter and
208 openings at the two-folds (Fig. 5B, C).

209

210 **Cryo-EM shows that faf-BSA or ion treatment of CVA9 leads to A-particle formation**

211 To evaluate structural changes in the CVA9 virions induced by different treatments, we solved cryo-
212 EM structures of the most populated classes from intact, faf-BSA treated and ion-treated CVA9 data
213 sets to 2.9, 3.5 and 3.3 Å resolution, respectively (Table 4; Fig. 6). The well-defined density of the
214 intact CVA9 virion shows features similar to those observed in capsids of other intact enteroviruses
215 and accommodates well the model for all four structural proteins of CVA9 obtained by X-ray
216 crystallography (PDB ID 1D4M) in a T=1 arrangement (29) (Fig. 6 and 7A). Similarly to the X-ray
217 structure, the intact virion reconstruction showed elongated density for a lipid factor placed in the
218 hydrophobic pocket in VP1 (Fig. 7A), as well as a large portion of the myristoyl group covalently
219 attached to the VP4 N-terminus. Furthermore, the base stacking interaction between vRNA and VP2
220 Trp38 next to the 2-fold axis inside the intact virion could be clearly observed (Fig. 7A). The average
221 radius of the intact virion, 15.6 nm, coincides well with the geometric radius measured in AF4
222 experiments (Table 2). Compared to the intact virions, the two cryo-EM reconstructions of CVA9
223 virions treated in two different ways, 0.01 % faf-BSA or ion composition, yielded RNA-containing A-
224 particles expanded by approximately 4% in diameter (Fig. 6 and 7B, C). In addition, these
225 reconstructions revealed more flexibility in capsid proteins and no density for the lipid factor. The
226 MS results indicated that there were only non-stoichiometric amounts of VP4 present and no VP4
227 could be modelled into the reconstructions (Fig. 7, Table 4). The internal density seen in the
228 difference map was attributed to vRNA (Fig. 7B and C).

229 Further comparison of the two expanded particle reconstructions showed subtle differences
230 between them (Fig. 7B and Fig. 7C). First, less of the VP1 N-terminus is ordered in the ion-treated
231 CVA9 where the first modelled residue is Ser60 compared to Lys54 in faf-BSA-treated CVA9 (Fig. 7).
232 The order of the E1 VP1 N-terminus after combined treatment is similar to that of faf-BSA treated
233 CVA9 (PDB ID: 6O06)(6). In addition, external loops of VP1 are missing Asp128-Asp136 residues in
234 faf-BSA and Asp128-Met137, Gln204, and Arg205 residues in ion-treated CVA9 models (Table 4). In
235 VP2, residues Cys28, Ala29 and Glu46-Ala49 in faf-BSA and Cys28, Asp44-Ala49, and Ala260 in ion-
236 treated CVA9 models are missing (Table 4). In VP3, surface exposed residues Tyr176-Glu183 in faf-
237 BSA and Tyr176-Tyr184 in ion-treated CVA9 models are missing (Table 4). Second, a poorly defined
238 density is seen on the ion-treated, but not BSA-treated, surface above the 2-fold opening (Fig. 7B,

239   C). The 3D classification of particles from ion-treated CVA9 refinement focused on the 2-fold

240   symmetry axis did not result in a better-defined density above the 2-fold opening, preventing a

241   detailed atomic interpretation (Fig. 4). Altogether cryo-EM reveals more flexibility in the ion-treated

242   compared to the faf-BSA-treated CVA9 capsid. This is in agreement with the fluorescence

243   measurements showing that ion treatment of CVA9 virions leads to more unstable A-particles,

244   which lose their vRNA becoming accessible to RNase (Fig. 1B blue lines). In contrast, the faf-BSA

245   treatment of CVA9 generates more stable A-particles as seen by fluorescence assay and AF4 (Fig. 1

246   and 2).

247   The average distribution of vRNA in the capsid changes with expansion (Fig. 6). In the intact virion,

248   the RNA is tethered to the capsid via the VP2 Trp38, but also is in close contact all over the capsid

249   interior. Following faf-BSA or ion-treatment, the average shape of the RNA expands, reflecting the

250   shape of the expanded capsid. However, apart from the tethering at the Trp38, the intimate contact

251   is lost (Fig 6). Electrostatic potential calculations for the capsid proteins in intact and expanded

252   virions indicate a significant shift to a much more negatively-charged surface inside the expanded

253   capsid generating repulsive vRNA-capsid interactions that could account for the observed changes

254   and contribute to vRNA exit (Fig. 8).

255

Discussion

257   In enteroviruses E1, E12 and coxsackievirus B3 serum albumin promotes virion expansion in a dose-

258   dependent manner by sequestering the lipid factor from the VP1 hydrophobic pocket as shown in

259   *in vitro* experiments (6, 20, 21). Here we studied and compared the roles of serum albumin and

260   endosomal ion concentrations at neutral pH in triggering CVA9 expansion and genome release. We

261   show that when used independently, both albumin and endosomal ion concentrations cause

262   particle expansion. However, the rate and extent of the order depend on the condition. The CVA9

263   treatment with albumin induces expansion in the majority of the particles exposing the VP1 N-

264   termini in about 30 min where most of the particles still contain vRNA (Fig. 1B, Fig. 2, Fig. 7B). The

265   ion treatment leads to a relatively slower particle expansion driving the capsid to a more disordered

266   state and the loss of vRNA from a significant population of particles (Fig. 1B, Fig 2, Fig. 7C, Table 4).

267   Both effects can be prevented by an excess of palmitate preventing the collapse of the VP1

268   hydrophobic pocket, a necessary event for expansion (Fig. 3B). When virions are treated with faf-

269   BSA, the lipid factor is bound more strongly by the albumin than by the capsid, causing the capsid

270 to expand. In the case of ion treatment, lipid factor dissociation from the particle might be driven

271 by changes in counter ions so that the vRNA swells, destabilizing the capsid for expansion.

272 A number of pieces of evidence indicate that the endosomes are the final location for picornavirus

273 uncoating and vRNA release into the cytosol (30-33). Our experiments support this idea by showing

274 that changes in cation concentrations to those mimicking the endosomal environment slowly

275 convert CVA9 into expanded virions. Moreover under these conditions, a significant fraction of the

276 virions lose their vRNA or dissociate completely as shown by AF4 and real-time fluorescence

277 measurements (Fig. 1 and 2). Viral RNA genomes inside the capsids are extremely compact despite

278 the repulsive negative charges of the RNA backbone phosphates (34). Tight vRNA folding depends

279 on both the RNA sequence specificity and the presence of cations, which compensate for the

280 repulsive interactions between negatively charged RNA backbones enabling close juxtaposition of

281 two phosphate groups. RNA phosphate oxyanions have significant affinity to Mg^{2+} due to its size

282 and charge density which allows small interatomic distances in RNA-Mg^{2+} clusters giving high

283 stability (35). RNA association with Na^+ and Ca^{2+} is not as stable, because of the smaller charge of

284 Na^+ and the bigger size of Ca^{2+} ions. The most abundant cations that associate with highly folded

285 RNAs are Mg^{2+} and Na^+ (36). As mentioned before, during endosome maturation there is a tendency

286 for decrease in Na^+ and Ca^{2+} ions and increase in K^+ ions (22, 23). There is no information about

287 changes in Mg^{2+} concentration in endosomes. Because of the changes in ion composition in

288 endosomes, K^+ ions might replace Na^+ and perhaps Mg^{2+} ions in the compact vRNA leading to

289 conformational changes and expansion or swelling of the vRNA. Furthermore, the comparison of

290 electrostatic potential on the internal surface of intact and expanded virions shows that vRNA-

291 capsid interactions become repulsive in expanded virions due to conformational changes and the

292 loss of much of the VP4, thus further fostering genome release (Fig. 8). In support of this, altered

293 vRNA-capsid interactions in an A-particle of human rhinovirus 2 have been described (37).

294 In conclusion, the enterovirus capsid expansion required for release of the genome in the endosome

295 can be triggered by albumin in the serum, but equally it can be triggered in a receptor- and acidic

296 pH-independent manner by the environment of the endosomal lumen.

297

298

Materials and methods

Virus production and purification

Green monkey kidney cells (GMK) were purchased from the American Type Culture Collection (ATCC) and were maintained in Eagle's minimum essential medium (MEM) supplemented with 10 % fetal bovine serum (FBS), 1 % GlutaMAX, and 1 % antibiotic–antimycotic solution in a chamber environment adjusted to 37 °C and 5 % CO_2. For CVA9 production semi-confluent 5-layer bottles of GMK cells were infected with CVA9 (ATCC, Griggs strain GenBank: D00627.1) using an MOI of 3.8 in medium containing 1 % FBS until total cell detachment (at 37 °C with 5 % CO_2 for 20 – 24 h). The cells and medium were collected, freeze-thawed three times and the cellular debris was centrifuged into a pellet (JA-10 rotor, 6080 rpm, 30 min, 4 °C). The virus containing supernatant was mixed with polyethylene glycol 6000 (Sigma Aldrich, Saint Louis, Missouri, US) (8 % wt/v) and NaCl (2.2% wt/v) at 4 °C overnight. The precipitate was pelleted (JA-10 rotor, 8000 rpm, 45 min, 4 °C) and resuspended in R-buffer (10 mM Tris-HCl (pH 7.5), 200 mM $MgCl_2$, 10 % (wt/v) glycerol). The resuspension was treated with 0.3 % (wt/v) sodium deoxylate (Sigma Aldrich) and 0.6 v/v Nonidet P-40 (Sigma Aldrich) for 30 min on ice and centrifuged (TX-200 rotor, 4700 rpm, 15 min, 4 °C) to pellet the remaining cellular membranes. The virus containing supernatant was loaded on top of linear 10 mL 5-20 % sucrose gradient prepared in R-buffer and centrifuged (SW-41 rotor, 35000 rpm, 2 h, 4 °C). The gradient was collected into 500 µL fractions and the virus containing fractions were detected using NanoDrop 1000 Spectrophotometer (Thermo Scientific, Waltham, Massachusetts, US). The virus containing sucrose fractions were diluted at least 1:5 in 2 mM $MgCl_2$-PBS and the virus was pelleted by centrifugation (70Ti rotor, 35000 rpm, 2 h, 4 °C) and resuspended in 2 mM $MgCl_2$-PBS. The concentration of the purified virus sample was measured using NanoDrop and the stock was stored at -80 °C in small aliquots.

^{35}S labelled virus production and purification

The 35S labelled virus was produced in semi-confluent 80 cm^2 cell culture bottles. The bottles were infected with CVA9 (ATCC, Griggs strain) in low-methionine-cysteine medium supplemented with 1 % FBS for three hours, after which the culture medium was changed into a low-methionine-cysteine medium supplemented with 1 % FBS containing 50 µCi/mL [^{35}S] methionine-cysteine. After total cell detachment (20 - 24 h) the cells were collected and freeze-thawed three times. After pelleting the

330 cellular residue (TX-200 rotor, 4000 rpm, 15 min, 4 °C) the supernatant was collected and Tween

331 was added in a final concentration of 0.1 %. Solution was incubated on ice for 30 min, centrifuged

332 (TX-200, 4700 rpm, 15min, 4 °C) and loaded on top of a 2 mL 40 % sucrose cushion on ice. The

333 cushion with the virus was centrifuged (SW-41, 30,000 rpm, 2.5 h, 4 °C), after which liquid above

334 the cushion and 500 μL fraction from the cushion was collected to waste and the remaining three

335 virus containing 500 μL fractions were diluted into 2 mM $MgCl_2$-PBS and the virus was pelleted (70Ti,

336 35000 rpm, 3 h, 4 °C). The pellet was resuspended into 1.5 mL of 2mM $MgCl_2$-PBS and separated in

337 5 - 20 % sucrose gradient in R-buffer (SW41, 35000 rpm, 2 h, 4 °C). After collecting 500 μL fractions,

338 the virus was identified using liquid scintillation analyzer TRI-carb 2910 TR (Perkin Elmer, Waltham,

339 Massachusetts, US). The virus containing fractions were collected and pelleted as earlier. The pellet

340 was dissolved in 2 mM PBS-$MgCl_2$ and stored at -80 °C in small aliquots.

341

342 **Analysis of treated CVA9 by ultracentrifugation in sucrose gradient**

343 1 μg of un-labelled purified CVA9 was mixed with 1 - 3 μL of ^{35}S labelled CVA9 (showing

344 approximately 1000 CPM) and faf-BSA (Sigma-Aldrich) or buffer giving final concentrations as

345 indicated in Table 1 was added to obtain final volume of 100 μL. For molar ratio calculations

346 between the pocket, faf-BSA and palmitate (Sigma-Aldrich), an estimated molecular weight of 8

347 MDa was used for CVA9 and the ones provided by the supplier for faf-BSA and palmitate. Samples

348 were incubated at 37 °C for 1 h (faf-BSA treatment) or 3 h (ion-treatment) before gradient

349 separation. The control samples (purified CVA9 in storage buffer, Table 1) were kept on ice during

350 the incubations. After the incubation the samples were pipetted on top of linear 5 - 20 % sucrose

351 gradients prepared in R-buffer and centrifuged (SW41, 35000 rpm, 2 h, 4 °C). After centrifugation,

352 500 μL fractions were collected and mixed with scintillation cocktail (Ultima Gold MW, Perkin Elmer)

353 and the radioactivity of each fraction was measured (Tri-Carb 2910 TR, Perkin Elmer).

354

355 **AF4**

356 The AF4 experiments were performed using the Eclipse NEON FFF system (Wyatt Technology, Santa

357 Barbara, USA) composed of Agilent 1260 Infinity II pump and autosampler, analytical long channel

358 with Dilution Control ModuleTM (Wyatt Technology, Santa Barbara, USA), and Agilent 1260 fraction

359 collector. AF4 device was coupled to Optilab® refractive index (dRI) detector (Wyatt Technology,

360 Santa Barbara, USA), DAWN multiangle light scattering detector (MALS) with 18 angles (Wyatt

361 Technology, Santa Barbara, USA), online dynamic light scattering detector (DLS) embedded in one

362 of the DAWN angles (Wyatt Technology, Santa Barbara, USA), and UV detector (Agilent) used at 280

363 nm. Regenerated cellulose membrane at 10 kDa cut off (Wyatt Technology, Santa Barbara, USA lot

364 RIJB19432) and Technology 525 μm spacer (Wyatt Technology, Santa Barbara, USA lot 247096) was

365 used as the accumulation wall. Focusing was performed at cross flow velocity of 2 mL/min. Sample

366 was injected at 0.2 mL/min. Elution was performed using constant cross flow velocity of 3 mL/min

367 for 80 min; channel flow was 1 mL/min; detector flow was 0.5 mL/min. The AF4 flows were

368 controlled via VISION 3.1 software (Wyatt Technology, Santa Barbara, USA). Channel temperature

369 was set to 25 °C. DPBS filtered through 0.1 μm filter was used as a mobile phase for all experiments.

370 Before sample runs, system set up was validated by running 30 μg of BSA solution (2 mg/mL). For

371 all experiments, sample corresponding to 10 μg of purified CVA9 was injected. ASTRA 8.1 software

372 was used for data analysis.

373 For AF4 analysis CVA9 was treated essentially the same way as for cryo-EM sample preparation.

374 Briefly, 12 μg of purified CVA9 (0.8 μg/μL) were mixed with faf-BSA at a final concentration of 0.01

375 % in DPBS giving 136 μL total volume. The sample was incubated either for 1 or 3 hours at 37 °C

376 prior to injecting to AF4 device. To analyse the effect of endosomal ionic content, purified CVA9

377 virions (12 μg) were incubated in ion-treatment buffer (136 μL total volume) for either 1 or 3 hours

378 at 37 °C and then analysed by AF4. Combined treatment was done by mixing purified CVA9 (12 μg)

379 with 0.01 % faf-BSA in ion-treatment buffer in 168 μL total volume and incubated for 1 hour at 37

380 °C, prior to AF4 analysis in 20 μL (for control), 140 μL (for ion-treated and combined treatment), or

381 113 μL (faf-BSA treated) volume.

382 Results obtained by multi-angle light scattering (MALS) and light scattering detectors were used to

383 calculate particle radius of gyration (Rg) and hydrodynamic radius (Rh), respectively. The Rg/Rh ratio

384 is between 0.75 and 0.82 indicating that shape of the particles present in different samples

385 corresponds to a hard sphere confirming expected particle shape in the peak fractions (Table 2) (38,

386 39).

387

388 **Real-time fluorescence measurements**

389 Conversion of CVA9 virions to expanded and empty or dissociated particles, which release their RNA,

390 was observed by real-time spectroscopy as described earlier (6, 27). In short, 1 μg of virus was mixed

391 with buffers containing different ion and supplement (faf-BSA, palmitate) concentrations in a

392 presence of 10X SYBR Green with or without RNase A. Buffer details are indicated in Table 1. The

393 total volume of each reaction mixture was 100 μL. The increase in fluorescence was observed using

394   PerkinElmer 2030 Multilabel Reader Victor X4 (Perkin Elmer) with F485 lamp filter and F535

395   emission filter for three hours at 37 °C, and the fluorescence with and without RNase was compared

396   to estimate whether the virus was in intact, expanded or dissociated form. A blank measurement

397   with all factors other than the virus was registered and subtracted from the corresponding values

398   obtained during the measurement with virus containing samples. The obtained fluorescence values

399   were normalised against the DPBS measurement and are shown in arbitrary units (AU).

400

401   **Liquid chromatography-mass spectrometry (LC-MS) analysis**

402   The peak fraction corresponding to the intact virions in AF4 run of untreated CVA9 (Fig. 2A) and the

403   peak fraction corresponding to the expanded virions in AF4 run of CVA9 after combined 0.01 % faf-

404   BSA and ion-treatment (Fig. 2F) were used for LC-MS analysis. First, each fraction (1 mL in total) was

405   heated at 60 °C for 5 min to inactivate the virus. Then 1 mL of lysis buffer (8 M Urea buffer, 50 mM

406   NH4HCO3, phosphatase inhibitors (Sigma-Aldrich, P2745), and protease inhibitors cocktail (Sigma-

407   Aldrich, P8340)) was added to each fraction on ice. Undissolved particles were removed by

408   centrifugation at 16,000 × g for 10 min at 4 °C. Samples were reduced with Tris(2-

409   carboxyethyl)phosphine (TCEP; Sigma Aldrich), and alkylated with iodoacetamide. Samples were

410   diluted with 50 mM ammonium bicarbonate (AMBIC; Sigma-Aldrich, 213-911-5) to reduce the urea

411   concentration to < 2 M. Sequencing Grade Modified Trypsin (Promega, PRV5111) was added to the

412   samples and incubated for 16 hours at 37 °C. Finally, the trypsin digested samples were desalted

413   with C18 BioPureSPN Mini columns (Nest Group, HUM S18V). A detailed description of the method

414   used here was previously published (40).

415   The desalted samples were analyzed using an EvoSep One liquid chromatography system coupled

416   with a hybrid trapped ion mobility quadrupole TOF mass spectrometer (Bruker timsTOF Pro2). The

417   samples were directly loaded on Evotips and separated with an 8 cm × 150 µm analytical column

418   (EV1109, Evosep) using the 60 samples per day method (21 min gradient time). Mobile phases A

419   and B were 0.1 % formic acid in water and 0.1 % formic acid in acetonitrile, respectively. The MS

420   analysis was performed in the positive-ion mode using data-dependent acquisition (DDA) in online

421   parallel accumulation-serial fragmentation (PASEF) mode (41) with 10 PASEF scans per topN

422   acquisition cycle. Raw data (.d) from timsTOF Pro were searched using MSFragger (42) against the

423   home-made CVA9 entries of the capsid proteins. Sequence of CVA9 Griggs isolate was used (43).

424   Carbamidomethylation of cysteine residues was used as static modification. Aminoterminal

425   acetylation and oxidation of methionine were used as the dynamic modification. Trypsin was

426   selected as enzyme, and maximum of two missed cleavages were allowed. Both instrument and

427   label-free quantification parameters were left to default settings.

428

429   **Cryo-EM sample preparation and data collection**

430   To analyse the effect of faf-BSA on CVA9 virion structure, 3 µg of purified CVA9 (0.8 µg/µL) were

431   mixed with faf-BSA at a final concentration of 0.01 % in DPBS giving 34 µL total volume. The sample

432   was incubated for 1 hour at 37 °C prior to plunging. To analyse the effect of endosomal ionic content

433   on CVA9 virion structure, purified CVA9 virions (3 µg) were incubated in ion-treatment buffer (34 µL

434   total volume) for 3 hours at 37 °C. For cryo-EM sample preparation, 3.0 µL of above-described

435   samples or non-treated CVA9 virions as a control were applied to glow-discharged grids (Quantifoil

436   R1.2/1.3 holey carbon on 300 copper mesh) that were manually blotted with filter paper and flash-

437   frozen in liquid ethane using a homemade plunger. Data was acquired at the Biocenter Finland

438   National Cryo-EM facility with a FEI TALOS Artica transmission electron microscope operated at 200

439   kV. Movies were collected with a Falcon III direct electron detector at a nominal magnification of

440   150 000x (for CVA9 control and CVA9 treated with faf-BSA) or 120 000x (for CVA9 treated with

441   endosomal ionic composition) giving a pixel size of 0.97 or 1.24 Å per pixel, respectively. Each movie

442   consisted of 30 frames with an exposure time of 1 second per frame. The total electron dose was

443   approximately 30 electrons per $Å^2$. Movies were corrected for beam-induced motion by aligning and

444   averaging all frames with Motioncor2 implemented in Scipion version 2.0 (44, 45).

445

446   **Image processing**

447   The contrast transfer function of the averaged micrographs was estimated by CTFFind4 in Scipion

448   version 2.0 (46, 47). Micrographs with astigmatism and diffraction were excluded from further

449   processing. For particle picking 2-step Xmipp3 was used from Scipion version 1.2, followed by 2D

450   classification in Relion 2 (48-50). Initial 3D models were generated using 2000, 1005 and 8012

451   particles for CVA9 control, CVA9 ion expanded and CVA9 BSA expanded, respectively, utilising 3D

452   initial model protocol in Relion 2 (49, 51, 52). Particles from the best 3D classes were further refined

453   and post-processed in Relion 2. After post-processing, particles were subjected to CTF-refinement

454   and Bayesian polishing using default parameters in Relion 3 (49, 51-54). Local resolution of the maps

455   was calculated in Relion 3 at 15 Å sampling rate and 25 Å resolution threshold for randomizing

456   phases (53, 55). However, at this stage, inspection of a 7530 particle reconstruction of the BSA-

457   treated CVA9 data set showed strong but poorly defined density beneath the capsid near the 5-fold

458　axis (Fig. 4). To try to resolve this 5f density we performed focused classification at the 5-fold

459　symmetry axis (Fig. 4). For this a cylindrical mask of 46 Å radius and 145 Å height was applied with

460　a centre shift below the 5-fold symmetry axis and only a small angular search was allowed (48, 56).

461　The focused 3D classification separated all particles into two well-defined classes. Classes were

462　further refined and post-processed in Relion 3 resolving characteristic features of expanded or

463　intact particles while the density below the 5-fold seen in the initial faf-BSA-treated CVA9

464　reconstruction disappeared and was attributed to VP4 density from contaminating intact particles

465　(Fig. 4). Approximately 18 % of all particles in the initial BSA-treated data set were found to be non-

466　expanded intact virions (Table 3). Similar results were obtained by 3D classification of the same set

467　of particles focused on a 2-fold symmetry axis by applying cylinder mask of 45 Å radius and 187 Å

468　height and shifting the centre of the mask so that capsid region at the 2-fold axis would be covered

469　(Fig. 4). A similar workflow of focused 3D classification was also applied to ion-treated CVA9 and

470　control data sets, but did not result in any other distinct classes other than the major class. Although

471　this procedure seemed to be robust in separating the intact and expanded particles, it was still not

472　sufficient. So additional rounds of inspection in UCSF Chimera, and classification in both 2D and 3D

473　were carried out, culminating in the identification of intact virions, non-expanded empty particles,

474　expanded virions and expanded empty particles. The majority particle type for the control and the

475　two treatments were then CTF refined and post-processed in Relion 3.

476　The FSC curve was calculated and the resolution of the final reconstructions was determined

477　according to the gold-standard FSC = 0.143 threshold criterion (57). The image processing and

478　refinement statistics for each data set are shown in Table 4 and the focused classification workflow

479　is shown in Fig 4.

480

481　**Modelling and analysis**

482　The CVA9 atomic model PDB ID 1D4M was fitted into the CVA9 control reconstruction using UCSF

483　Chimera 1.15 and manually adjusted in Coot 0.9.2 (58, 59). The initial model for the CVA9 A-particle

484　was a homology model calculated in I-Tasser using the expanded E1 particle PDB ID 6O06 as a

485　reference (6, 60). I-Tasser derived models were fitted into the density maps of faf-BSA treated and

486　ion treated CVA9 using UCSF Chimera 1.15 and were manually adjusted in Coot 0.9.2. Residues for

487　which densities were not observed in the cryo-EM maps, were deleted as indicated in Table 4. All

488　three optimized models were further refined against the cryo-EM map in Molecular Dynamics

489　Flexible Fitting (MDFF) program operating together with NAMD and VMD (61-63). A scale factor of

490 1 was used to weigh the contribution of the cryo-EM map to the overall potential function used in

491 MDFF. Simulations included 10,000 steps of minimization and 100,000 steps of molecular dynamics

492 under implicit solvent conditions with secondary structure restraints in place. The refined models
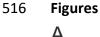
493 were validated using the MolProbity server (64).

494 Comparison of the maps was done in UCSF Chimera 1.15 by implementing "subtract maps" feature.

495 The maps were calculated at the same resolution and threshold value. Unmodelled densities were

496 identified by creating a density map around the atomic model with the "molmap" command and

497 subtracting it from the corresponding reconstruction.

498

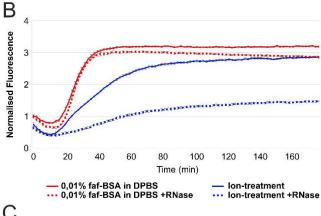499 **Calculations of electrostatic potential of capsid proteins**

500 Final atomic models of capsid proteins of intact and faf-BSA treated CVA9 were used for calculations

501 of electrostatic potential. PDB files were converted to PQR using the PDB2PQR online tool

502 (https://server.poissonboltzmann.org/pdb2pqr) with PROPKA at pH 7.0 to assign protonation states

503 with CHARMM force field and leaving additional options as the default settings. Output results were

504 used for Adaptive Poisson-Boltzmann Solver (APBS) calculations with the Poisson-Boltzmann

505 equation (65). Input parameters were left as the default settings. The output PQR file was used for

506 visualization in ChimeraX 1.3 (66, 67). Surface representation of the input asymmetric subunit PDB

507 file was colored based on the PQR file electrostatic potential values in a range from -10 to 10 from

508 the mean.

509

510 **Data availability**

511 The atomic models and cryo-EM maps generated during the current study are available in the

512 wwPDB repositories with accession numbers PDB ID 8AT5, EMD-15634 (CVA9 control), PDB ID

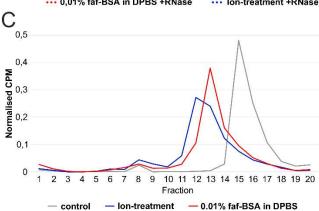513 8AW6, EMD-15692 (faf-BSA-treated CVA9) and PDB ID 8AXX, EMD-15706 (ion-treated CVA9).

514

515

516 **Figures**

Figure 1. Endosomal ion and 0.01 % faf-BSA treatment, individually or in combination, leads to CVA9 virion expansion. **(A)** Real-time spectroscopy measurements of fluorescent dye SYBR Green II accessibility to CVA9 genome in the presence of 0.01 % faf-BSA in endosomal ionic environment (green) with (dotted line) or without RNase (solid line). Untreated CVA9 in DPBS (black) with (dotted line) or without RNase (solid line) was used as a control. **(B)** Real-time spectroscopy measurements of fluorescent dye SYBR Green II accessibility to CVA9 genome in the presence of 0.01 % faf-BSA (red) or endosomal ion composition (blue) with (dotted line) or without RNase (solid line). The fluorescence signal under the dotted curve indicates expanded virions, whereas fluorescence signal between solid and dotted curves originates from released genome, i.e. empty capsids. **(C)** Effect of

527   0.01 % faf-BSA and endosomal ions on metabolically labeled ^{35}S CVA9 virions as analyzed by

528   ultracentrifugation in 5 % to 20 % sucrose gradient and subsequent fractionation. CVA9 after

529   endosomal ionic treatment (blue) and 0.01 % faf-BSA treatment (red) are shown. Non-treated CVA9

530   in PBS-Mg buffer was used as a control (grey). Intact viruses are observed mainly in fractions 15 -

531   16, intermediate particles mainly in fractions 12 - 13 and empty particles in fractions 8 - 10. The

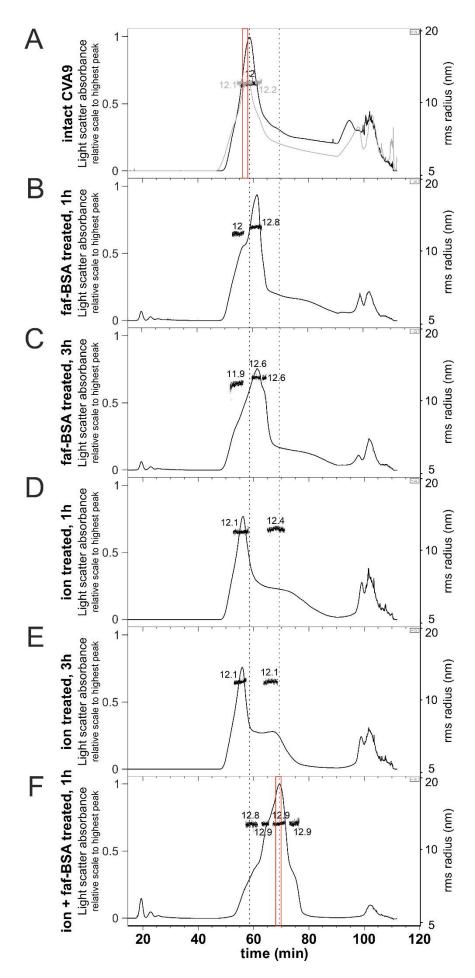532   exact buffer composition is given in Table 1.

534

535   **Figure 2.** AF4 allows separation of heterogeneous CVA9 virion population generated by 0.01 % faf-

536   BSA and endosomal ion-treatment. **(A)** Two independent AF4 fractograms of untreated CVA9. **(B)**

537   AF4 fractogram of CVA9 after 1 hour treatment with 0.01 % faf-BSA at 37 °C. **(C)** AF4 fractogram of

538   CVA9 after 3 hour treatment with 0.01 % faf-BSA at 37 °C. **(D)** AF4 fractogram of CVA9 after 1 hour

539   treatment in endosomal ion environment at 37 °C. **(E)** AF4 fractogram of CVA9 after 3 hour

540   treatment in endosomal ion environment at 37 °C. **(F)** AF4 fractogram of CVA9 after combined

541   treatment (0.01 % faf-BSA in endosomal ionic environment) for 1 hour at 37 °C. In all panels, x axis

542   indicates time, 1-mL fractions were collected at the rate of 0.5 mL/min; y axis on the left shows light

543   scattering (black or grey lines), and on the right hydrodynamic radius is shown as measured by

544   online dynamic light scattering detector (black dots). Vertical dashed line on the left indicates peak

545   for intact and on the right peak for expanded particles. AF4 fractions used for MS analysis are

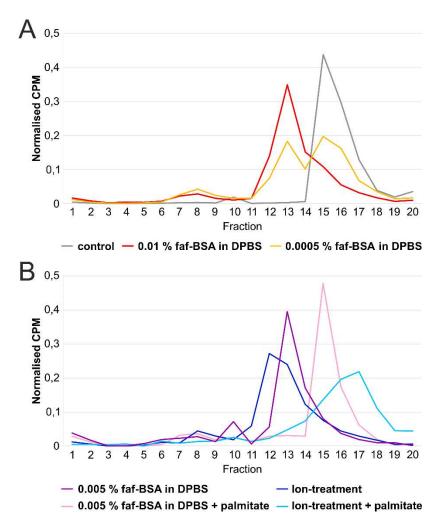546   indicated by red boxes.

547

548

549

Figure 3. CVA9 expansion dependency on faf-BSA and palmitate concentrations. **(A)** Fractionation of untreated (grey), 0.01 % faf-BSA (red) or 0.0005 % faf-BSA (orange) treated CVA9 after separation in 5 % to 20 % sucrose gradient using ultracentrifugation. Peak for intact virions corresponds to fractions 15 - 17, for expanded virions to fractions 12 - 14, and empty virions to fractions 7 - 10. **(B)** Analysis of CVA9 treated with 0.005 % faf-BSA in the presence of excess of palmitate (pink) after ultracentrifugation in 5 % to 20 % sucrose gradient. For comparison, 0.005 % faf-BSA treated CVA9 ultracentrifuged the same way without addition of palmitate is shown (purple). Similar analysis of CVA9 treated with endosomal ion concentrations with (blue) or without addition of palmitate (light blue) is also shown. Peak for intact virions corresponds to fractions 15 - 18, for expanded virions to fractions 12 - 14, and empty capsids to fractions 7 - 10. Buffer composition is shown in Table 1.
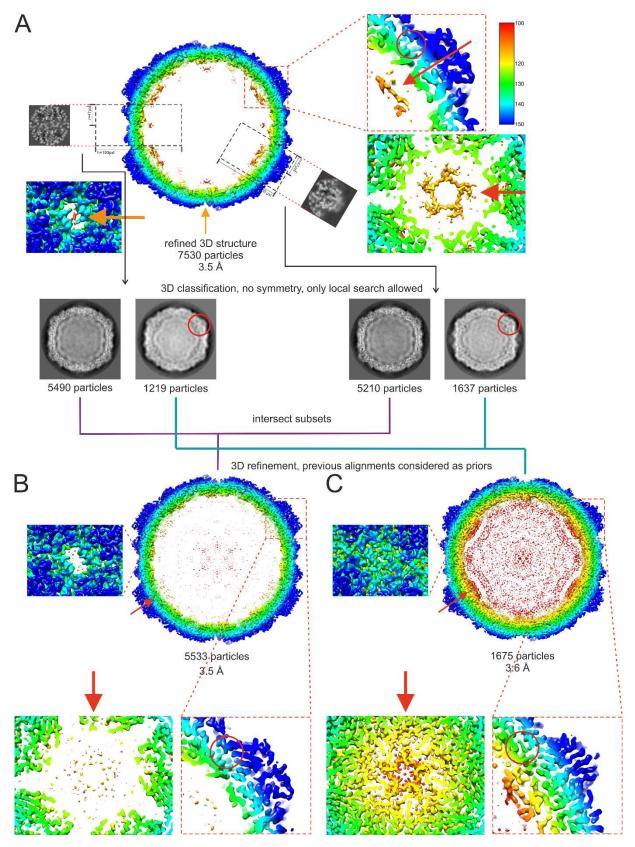
Figure 4: Workflow of focused classification applied to the faf-BSA treated CVA9 dataset to sort heterogeneity. **A.** Cross section of an initial faf-BSA treated CVA9 reconstruction using standard 2D and 3D classifications. Features of interest at 2-fold and 5-fold are enlarged as well as the position of the hydrophobic pocket. Despite the nominal resolution of 3.5 Å resolution, the density under

565   the 5f was much more ordered than expected. Focused classification on either 2-fold or 5-fold

566   yielded two distinct classes corresponding to intact and expanded particles ordered density was

567   due to contamination with virion particles in the reconstruction. The consensus classes were used

568   for further refinement. **B.** Cross section of the faf-BSA expanded CVA9 particle density map.

569   Features at 2-fold, 5-fold and the collapsed hydrophobic pocket are enlarged. **C.** Cross section of

570   the native CVA9 particle density map obtained from a 2D class in faf-BSA treated CVA9 dataset**. A-**

571   **C**. Features at 2-fold, 5-fold and the collapsed hydrophobic pocket are enlarged. Density maps are

572   radially colored in Å from center according to the color key on the right in **A**. Red circles indicate

573   the position of VP1 where the hydrophobic pocket is occupied in the virion, but collapsed in the

574   expanded particle. Red arrows indicate representations where VP4 is organized in the virion, but

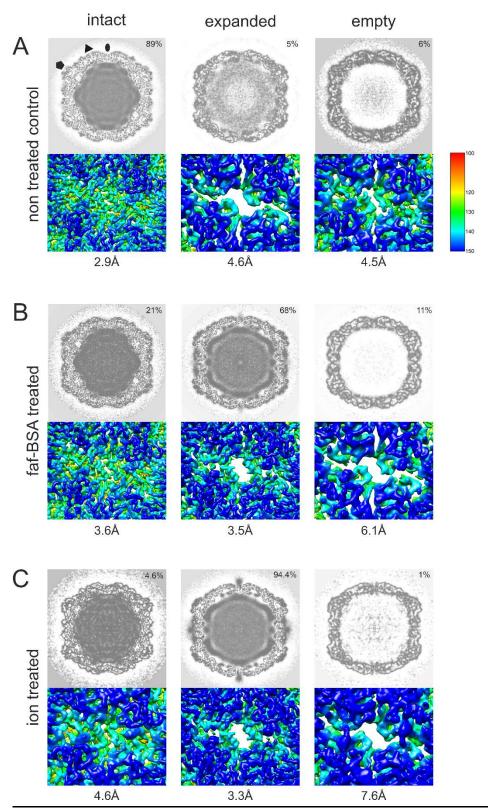575   missing in the expanded particles.

576

Figure 5. Heterogeneity of CVA9 virions in different data sets after cryo-EM and single particle analysis. **(A)** Analysis of data set of untreated CVA9 resulted in intact, empty non-expanded and expanded virions containing the genome. **(B)** Data set of 0.01 % faf-BSA treated CVA9 separated into expanded empty and filled capsids and in addition to intact particles. **(C)** CVA9 after treatment with endosomal ionic concentrations, in addition to main class of genome-containing expanded

583   virions, yielded small population of intact virions and expanded empty capsids. In all panels, top

584   view shows central plane of the refined reconstructions, and below the enlarged view of a surface

585   representation of a reconstruction is shown at 2-fold axis clearly indicating opening seen in

586   expanded virions. Distribution of particle classes is indicated on the top right corner and resolution

587   of the reconstruction is shown below the figure. Reconstructions are colored according to radial

588   distance in Å from the particle center (color key shown on the left) and shown at 3 σ above mean.
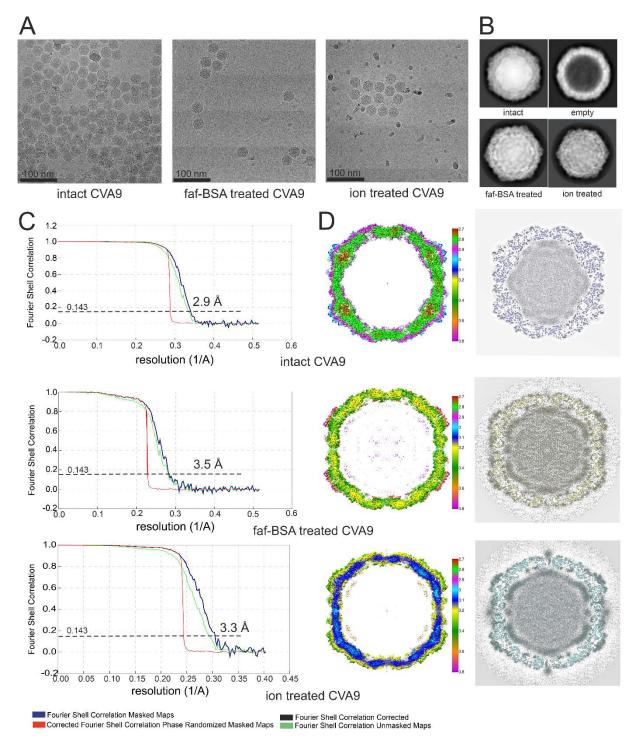
589

Figure 6. Cryo-EM data collection and single particle analysis. **(A)** Representative micrographs from untreated, 0.01 % faf-BSA and endosomal ionic conditions treated CVA9 data sets. Scale bar, 100 nm. **(B)** Example 2D class averages obtained in Relion 2 during processing workflow for three data sets; 2D class average corresponding to empty virions is from untreated CVA9 data set. **(C)** FSC curves of final reconstructions for intact CVA9, 0.01 % faf-BSA-treated and endosomal ion-treated CVA9 and estimated resolutions at 0.143 threshold. **(D)** Left, central sections of the CVA9

598   reconstructions colored according to local resolution as shown by the color keys (in Å).

599   Reconstructions are shown at 2 σ above mean. On the right, central planes of the reconstructions
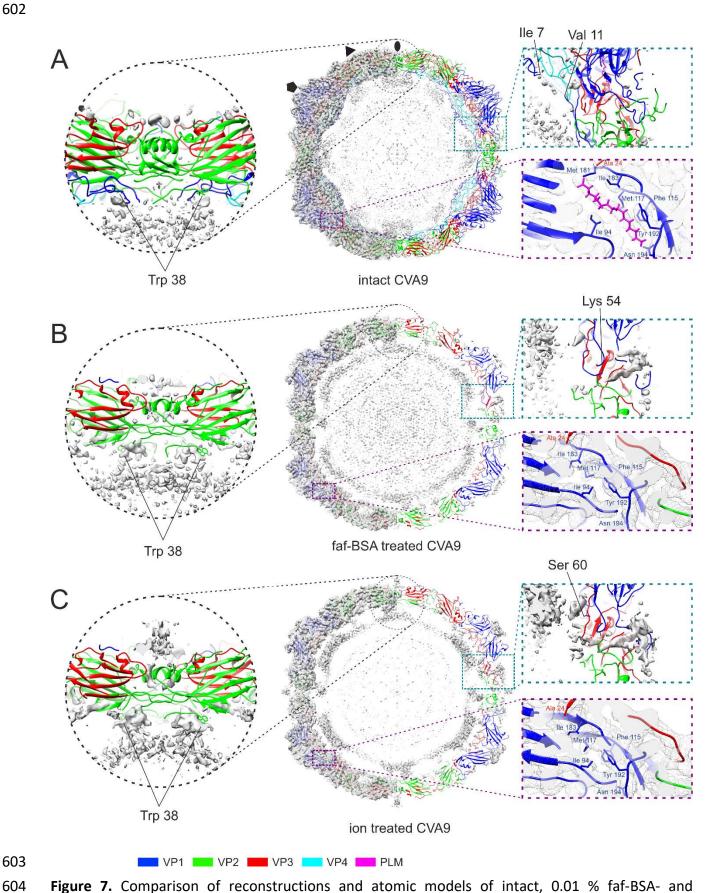
600   are shown.

601

602

Figure 7. Comparison of reconstructions and atomic models of intact, 0.01 % faf-BSA- and endosomal ion-treated CVA9 virions. **(A)** Untreated CVA9 central section through the model fitted

606   into the reconstruction shown at 3 σ above mean. Left half, cryoEM density with atomic model fit;

607   right half, the cryoEM density accounted for by the atomic model is not shown to reveal the un-

608   modelled density. Symmetry axes are marked as follows, 5-fold (pentagon), 3-fold (triangle) and 2-

609   fold (ellipse). Enlarged view of the model at a 2-fold symmetry axis highlights the vRNA contacts

610   with Trp 38 from VP2 observed in all three reconstructions. Enlarged view on the right shows that

611   most of the density in the capsid region is accounted for. VP1 N-terminus extends on the inside of

612   the capsid hugging VP4 and density for a lipid factor can accommodate an atomic model of a

613   palmitate. **(B)** Central section through the atomic model fitted into the reconstruction of 0.01 % faf-

614   BSA treated CVA9. On the right, half of the density that was accounted by an atomic model was

615   removed to better visualize the un-modelled density. Enlarged view of vRNA contacts with Trp 38

616   from VP2 is shown. View of un-modelled density near the VP1 N-terminus (Lys 54) spanning the

617   capsid of expanded virions and collapsed hydrophobic pocket are zoomed on the right. **(C)** Central

618   section through the atomic model fitted into the reconstruction of endosomal ion-treated CVA9. On

619   the right, half of the density that was accounted by an atomic model was removed to better visualize

620   the un-modelled density. Enlarged view of vRNA contacts with Trp 38 from VP2 is shown in which

621   the density above 2-fold can also be seen. View of un-modelled density near the VP1 N-terminus

622   (Ser 60) spanning the capsid of expanded virions and collapsed hydrophobic pocket are zoomed on
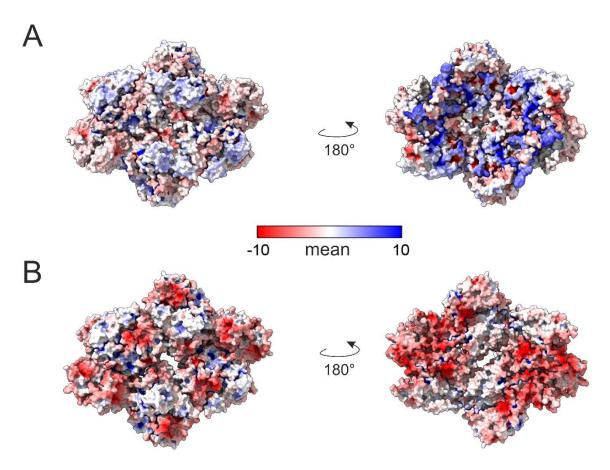
623   the right.

Figure 8. Calculations of electrostatic potentials show significant change from a positive to a negative charge at the inner surface of the capsid when intact and expanded virions are compared. Electrostatic potentials calculated for an asymmetric unit shown for outer (left) and inner (right) surface of untreated **(A)** and 0.01 % faf-BSA treated CVA9 **(B)** as a colored surface according to a color key. Four subunits around 2-fold axis are shown.

Tables

Table 1. Final buffer compositions used for treating CVA9 virions.

Buffer[a]	NaCl	Na$_2$HPO$_4$	total Na	KCl	KH$_2$PO$_4$	K$_2$HPO$_4$	total K	MgCl$_2$	CaCl$_2$	faf-BSA (µM)	Palmitate (µM)
PBS-Mg (storage)	137	8	153	3	2	-	5	2	-	-	
DPBS	138	8.1	154.2	2.7	1.5	-	4.2	0.5	0.9	-	-
Ion treatment	20	-	20	-	6	12	30	0.5	0.45	-	-
Ion treatment, 15 µM palmitate	20	-	20	-	6	12	30	0.5	0.45	-	15
0.01 % faf-BSA[b]	138	8.1	154.2	2.7	1.5	-	4.2	0.5	0.9	1.52	-
0.005 % faf-BSA	138	8.1	154.2	2.7	1.5	-	4.2	0.5	0.9	0.75	-
0.0005 % faf-BSA	138	8.1	154.2	2.7	1.5	-	4.2	0.5	0.9	0.075	-
0.005 % faf-BSA, 15 µM palmitate	138	8.1	154.2	2.7	1.5	-	4.2	0.5	0.9	0.75	15
0.01 % faf-BSA in ion buffer (combined)	20	-	20	-	6	12	30	0.5	0.45	1.52	-

[a] if not indicated, concentrations are given in mM

[b] 0.01% faf-BSA corresponds to 20-fold excess of faf-BSA molecules per hydrophobic pocket in the virion (60 pockets per virus), when 10 µg/mL of CVA9 is used. This gives approximately 1.25 nM concentration of CVA9 with estimated MW of the virion of 8MDa.

Table 2. AF4 Results

CVA9 treatment	Rh, nm	Rg, nm	Rg/Rh	R, nm
no treatment (control)	14.8	12.1	0.82	15.6
faf-BSA 1h	17.0	12.8	0.75	16.5
faf-BSA 3h	16.7	12.6	0.75	16.3
ions 1h	14.7	12.1	0.82	15.6
ions 3h	14.7	12.1	0.82	15.6
combined treatment 1h	17.0	12.9	0.76	16.7

Rh, hydrodynamic radius; Rg, radius of gyration; R, geometric radius.

Geometric radius has been estimated using following equation:

$(Rg)^2 = 3/5 R^2$

648 **Table 3. Particle heterogeneity**

649

type of particles	native CVA9	BSA-treated CVA9	ion-treated CVA9
total number of particles	21 365	8 061	9 055
empty particles	1 275^	853*	93*
expanded particles	1 024	5 533	8 540
non-expanded particles	19 066	1 675	422

650

651 * expanded particles

652 ^ non-expanded particles

653

654 **Table 4. Cryo-EM data collection, refinement and validation statistics**

655

	CVA9	CVA9-ion treatment	CVA9-BSA treatment
Data collection and processing			
Magnification	150000	120000	150000
Voltage (kV)	200	200	200
Electron exposure (e–/Å²)	30	30	30
Defocus range settings (μm)	-0.8 – 1.8	-0.6 – 1.8	-0.8 – 1.8
Pixel size (Å)	0.97	1.24	0.97
Symmetry imposed	I2	I2	I2
Micrographs (no.)	2421	1964	2472
Initial particle images (no.)	28818	9702	15179
Good particles	21365	9055	8061
Final particle images (no.)	19066	8540	5533
Map resolution (Å)	2.9	3.3	3.5
FSC threshold	0.143	0.143	0.143
Map resolution range (Å)	999-1.94	999-2.48	999-1.94
Refinement			
Map sharpening *B* factor (Å²)	-50	-70	-70
Model composition			
Non-hydrogen atoms			
Protein residues			
VP1	1-7, 11-283	60-127, 138-203, 206-283	54-127, 137-282
VP2	10-260	14-27, 29-43, 50-259	14-27, 30-45, 50-260
VP3	1-238	3-175, 185-233	3-175, 184-233
VP4	MYR-1-14, 23-68	-	-
Ligands	Lipid factor	-	-
R.m.s. deviations			
Bond lengths (Å)	0.67	0.88	0.87
Bond angles (°)	0.67	1.00	0.99
Validation			
MolProbity score	1.74	1.27	1.19
Clashscore	0.9	0	0
Poor rotamers (%)	4.85	2.05	1.65
Ramachandran plot			
Favored (%)	89.83	90.72	90.91
Allowed (%)	8.33	5.86	7.18
Disallowed (%)	1.84	3.42	1.91

Acknowledgements

Author contributions

S.J.B. and V.M. conceived the idea. S.J.B., V.M, A.D. designed the experiments. A.D. B.L., Z.P., and V.R. carried out the experiments. A.D., Z.P., B.L. did image analysis. Z.P. and A.D. built the atomic models. V.R. and Z.P prepared the figures. Z.P, V.R., A.D. and S.J.B. interpreted the results. A.D., V.R. and S.J.B. wrote the manuscript. All authors edited and agreed on the final manuscript.

Competing interests

The authors declare no competing interests.

References

1.   Aldriweesh MA, Shafaay EA, Alwatban SM, Alkethami OM, Aljuraisi FN, Bosaeed M, et al. Viruses Causing Aseptic Meningitis: A Tertiary Medical Center Experience With a Multiplex PCR Assay. Front Neurol. 2020;11:602267.

688 2.   Huang YC, Chu YH, Yen TY, Huang WC, Huang LM, Cheng AL, et al. Clinical features
689 and phylogenetic analysis of Coxsackievirus A9 in Northern Taiwan in 2011. BMC Infect Dis.
690 2013;13:33.
691 3.   Lafolie J, Labbe A, L'Honneur AS, Madhi F, Pereira B, Decobert M, et al. Assessment of
692 blood enterovirus PCR testing in paediatric populations with fever without source, sepsis-like
693 disease, or suspected meningitis: a prospective, multicentre, observational cohort study. Lancet
694 Infect Dis. 2018;18(12):1385-96.
695 4.   Shabani A, Makvandi M, Samarbafzadeh A, Teimoori A, Rasti M, Karami C, et al.
696 Echovirus 30 and coxsackievirus A9 infection among young neonates with sepsis in Iran. Iran J
697 Microbiol. 2018;10(4):258-65.
698 5.   Jiang P, Liu Y, Ma HC, Paul AV, Wimmer E. Picornavirus morphogenesis. Microbiol Mol
699 Biol Rev. 2014;78(3):418-37.
700 6.   Ruokolainen V, Domanska A, Laajala M, Pelliccia M, Butcher SJ, Marjomaki V.
701 Extracellular Albumin and Endosomal Ions Prime Enterovirus Particles for Uncoating That Can Be
702 Prevented by Fatty Acid Saturation. J Virol. 2019;93(17).
703 7.   Zhang P, Mueller S, Morais MC, Bator CM, Bowman VD, Hafenstein S, et al. Crystal
704 structure of CD155 and electron microscopic studies of its complexes with polioviruses. Proc Natl
705 Acad Sci U S A. 2008;105(47):18284-9.
706 8.   Ren J, Wang X, Hu Z, Gao Q, Sun Y, Li X, et al. Picornavirus uncoating intermediate
707 captured in atomic detail. Nat Commun. 2013;4:1929.
708 9.   Liu Y, Sheng J, Baggen J, Meng G, Xiao C, Thibaut HJ, et al. Sialic acid-dependent cell
709 entry of human enterovirus D68. Nat Commun. 2015;6:8865.
710 10.   Strauss M, Schotte L, Karunatilaka KS, Filman DJ, Hogle JM. Cryo-electron Microscopy
711 Structures of Expanded Poliovirus with VHHs Sample the Conformational Repertoire of the
712 Expanded State. J Virol. 2017;91(3).
713 11.   Danthi P, Tosteson M, Li QH, Chow M. Genome delivery and ion channel properties are
714 altered in VP4 mutants of poliovirus. J Virol. 2003;77(9):5266-74.
715 12.   Smyth M, Pettitt T, Symonds A, Martin J. Identification of the pocket factors in a
716 picornavirus. Arch Virol. 2003;148(6):1225-33.
717 13.   Rossmann MG, He Y, Kuhn RJ. Picornavirus-receptor interactions. Trends Microbiol.
718 2002;10(7):324-31.
719 14.   Milstone AM, Petrella J, Sanchez MD, Mahmud M, Whitbeck JC, Bergelson JM.
720 Interaction with coxsackievirus and adenovirus receptor, but not with decay-accelerating factor
721 (DAF), induces A-particle formation in a DAF-binding coxsackievirus B3 isolate. J Virol.
722 2005;79(1):655-60.
723 15.   Huttunen M, Waris M, Kajander R, Hyypia T, Marjomaki V. Coxsackievirus A9 infects
724 cells via nonacidic multivesicular bodies. J Virol. 2014;88(9):5138-51.
725 16.   Myllynen M, Kazmertsuk A, Marjomaki V. A Novel Open and Infectious Form of
726 Echovirus 1. J Virol. 2016;90(15):6759-70.
727 17.   Shakeel S, Seitsonen JJ, Kajander T, Laurinmaki P, Hyypia T, Susi P, et al. Structural and
728 functional analysis of coxsackievirus A9 integrin alphavbeta6 binding and uncoating. J Virol.
729 2013;87(7):3943-51.
730 18.   Karjalainen M, Rintanen N, Lehkonen M, Kallio K, Maki A, Hellstrom K, et al. Echovirus 1
731 infection depends on biogenesis of novel multivesicular bodies. Cell Microbiol. 2011;13(12):1975-
732 95.
733 19.   Baggen J, Thibaut HJ, Strating J, van Kuppeveld FJM. The life cycle of non-polio
734 enteroviruses and how to target it. Nat Rev Microbiol. 2018;16(6):368-81.
735 20.   Ward T, Powell RM, Chaudhry Y, Meredith J, Almond JW, Kraus W, et al. Fatty acid-
736 depleted albumin induces the formation of echovirus A particles. J Virol. 2000;74(7):3410-2.

737 21.   Carson SD, Cole AJ. Albumin Enhances the Rate at Which Coxsackievirus B3 Strain 28
738 Converts to A-Particles. J Virol. 2020;94(6).
739 22.   Raiborg C, Bache KG, Gillooly DJ, Madshus IH, Stang E, Stenmark H. Hrs sorts
740 ubiquitinated proteins into clathrin-coated microdomains of early endosomes. Nat Cell Biol.
741 2002;4(5):394-8.
742 23.   Scott CC, Gruenberg J. Ion flux and the function of endosomes and lysosomes: pH is just
743 the start: the flux of ions across endosomal membranes influences endosome function not only
744 through regulation of the luminal pH. Bioessays. 2011;33(2):103-10.
745 24.   Gerasimenko JV, Tepikin AV, Petersen OH, Gerasimenko OV. Calcium uptake via
746 endocytosis with rapid release from acidifying endosomes. Curr Biol. 1998;8(24):1335-8.
747 25.   Christensen KA, Myers JT, Swanson JA. pH-dependent regulation of lysosomal calcium in
748 macrophages. J Cell Sci. 2002;115(Pt 3):599-607.
749 26.   Steinberg BE, Huynh KK, Brodovitch A, Jabs S, Stauber T, Jentsch TJ, et al. A cation
750 counterflux supports lysosomal acidification. J Cell Biol. 2010;189(7):1171-86.
751 27.   Ruokolainen V, Laajala M, Marjomaki V. Real-time Fluorescence Measurement of
752 Enterovirus Uncoating. Bio Protoc. 2020;10(7):e3582.
753 28.   Curry S, Chow M, Hogle JM. The poliovirus 135S particle is infectious. J Virol.
754 1996;70(10):7125-31.
755 29.   Hendry E, Hatanaka H, Fry E, Smyth M, Tate J, Stanway G, et al. The crystal structure of
756 coxsackievirus A9: new insights into the uncoating mechanisms of enteroviruses. Structure.
757 1999;7(12):1527-38.
758 30.   Brandenburg B, Lee LY, Lakadamyali M, Rust MJ, Zhuang X, Hogle JM. Imaging
759 poliovirus entry in live cells. PLoS Biol. 2007;5(7):e183.
760 31.   Brabec M, Schober D, Wagner E, Bayer N, Murphy RF, Blaas D, et al. Opening of size-
761 selective pores in endosomes during human rhinovirus serotype 2 in vivo uncoating monitored by
762 single-organelle flow analysis. J Virol. 2005;79(2):1008-16.
763 32.   Strauss M, Levy HC, Bostina M, Filman DJ, Hogle JM. RNA transfer from poliovirus 135S
764 particles across membranes is mediated by long umbilical connectors. J Virol. 2013;87(7):3903-14.
765 33.   Bilek G, Matscheko NM, Pickl-Herk A, Weiss VU, Subirats X, Kenndler E, et al.
766 Liposomal nanocontainers as models for viral infection: monitoring viral genomic RNA transfer
767 through lipid membranes. J Virol. 2011;85(16):8368-75.
768 34.   Tubiana L, Bozic AL, Micheletti C, Podgornik R. Synonymous mutations reduce genome
769 compactness in icosahedral ssRNA viruses. Biophys J. 2015;108(1):194-202.
770 35.   Petrov AS, Bowman JC, Harvey SC, Williams LD. Bidentate RNA-magnesium clamps: on
771 the origin of the special role of magnesium in RNA folding. RNA. 2011;17(2):291-7.
772 36.   Draper DE. Folding of RNA tertiary structure: Linkages between backbone phosphates,
773 ions, and water. Biopolymers. 2013;99(12):1105-13.
774 37.   Pickl-Herk A, Luque D, Vives-Adrian L, Querol-Audi J, Garriga D, Trus BL, et al.
775 Uncoating of common cold virus is preceded by RNA switching as determined by X-ray and cryo-
776 EM analyses of the subviral A-particle. Proc Natl Acad Sci U S A. 2013;110(50):20063-8.
777 38.   Guo P, Li Y, An J, Shen S, Dou H. Study on structure-function of starch by asymmetrical
778 flow field-flow fractionation coupled with multiple detectors: A review. Carbohydr Polym.
779 2019;226:115330.
780 39.   Kotoucek J, Hezova R, Vrablikova A, Hubatka F, Kulich P, Macaulay S, et al.
781 Characterization and purification of pentameric chimeric protein particles using asymmetric flow
782 field-flow fractionation coupled with multiple detectors. Anal Bioanal Chem. 2021;413(14):3749-
783 61.
784 40.   Liu X, Salokas K, Weldatsadik RG, Gawriyski L, Varjosalo M. Combined proximity
785 labeling and affinity purification-mass spectrometry workflow for mapping and visualizing protein
786 interaction networks. Nat Protoc. 2020;15(10):3182-211.

787   41.   Meier F, Brunner AD, Koch S, Koch H, Lubeck M, Krause M, et al. Online Parallel
788   Accumulation-Serial Fragmentation (PASEF) with a Novel Trapped Ion Mobility Mass
789   Spectrometer. Mol Cell Proteomics. 2018;17(12):2534-45.
790   42.   Yu F, Haynes SE, Teo GC, Avtonomov DM, Polasky DA, Nesvizhskii AI. Fast Quantitative
791   Analysis of timsTOF PASEF Data with MSFragger and IonQuant. Mol Cell Proteomics.
792   2020;19(9):1575-85.
793   43.   Chang KH, Auvinen P, Hyypia T, Stanway G. The nucleotide sequence of coxsackievirus
794   A9; implications for receptor binding and enterovirus classification. J Gen Virol. 1989;70 (Pt
795   12):3269-80.
796   44.   Zheng SQ, Palovcak E, Armache JP, Verba KA, Cheng Y, Agard DA. MotionCor2:
797   anisotropic correction of beam-induced motion for improved cryo-electron microscopy. Nat
798   Methods. 2017;14(4):331-2.
799   45.   de la Rosa-Trevin JM, Quintana A, Del Cano L, Zaldivar A, Foche I, Gutierrez J, et al.
800   Scipion: A software framework toward integration, reproducibility and validation in 3D electron
801   microscopy. J Struct Biol. 2016;195(1):93-9.
802   46.   Rohou A, Grigorieff N. CTFFIND4: Fast and accurate defocus estimation from electron
803   micrographs. J Struct Biol. 2015;192(2):216-21.
804   47.   Mindell JA, Grigorieff N. Accurate determination of local defocus and specimen tilt in
805   electron microscopy. J Struct Biol. 2003;142(3):334-47.
806   48.   de la Rosa-Trevin JM, Oton J, Marabini R, Zaldivar A, Vargas J, Carazo JM, et al. Xmipp
807   3.0: an improved software suite for image processing in electron microscopy. J Struct Biol.
808   2013;184(2):321-8.
809   49.   Scheres SH. RELION: implementation of a Bayesian approach to cryo-EM structure
810   determination. J Struct Biol. 2012;180(3):519-30.
811   50.   Abrishami V, Zaldivar-Peraza A, de la Rosa-Trevin JM, Vargas J, Oton J, Marabini R, et al.
812   A pattern matching approach to the automatic selection of particles from low-contrast electron
813   micrographs. Bioinformatics. 2013;29(19):2460-8.
814   51.   Scheres SH. A Bayesian view on cryo-EM structure determination. J Mol Biol.
815   2012;415(2):406-18.
816   52.   Kimanius D, Forsberg BO, Scheres SH, Lindahl E. Accelerated cryo-EM structure
817   determination with parallelisation using GPUs in RELION-2. Elife. 2016;5.
818   53.   Zivanov J, Nakane T, Forsberg BO, Kimanius D, Hagen WJ, Lindahl E, et al. New tools for
819   automated high-resolution cryo-EM structure determination in RELION-3. Elife. 2018;7.
820   54.   Scheres SH. Beam-induced motion correction for sub-megadalton cryo-EM particles. Elife.
821   2014;3:e03665.
822   55.   Chen Y, Pfeffer S, Hrabe T, Schuller JM, Forster F. Fast and accurate reference-free
823   alignment of subtomograms. J Struct Biol. 2013;182(3):235-45.
824   56.   Sorzano CO, de la Rosa Trevin JM, Oton J, Vega JJ, Cuenca J, Zaldivar-Peraza A, et al.
825   Semiautomatic, high-throughput, high-resolution protocol for three-dimensional reconstruction of
826   single particles in electron microscopy. Methods Mol Biol. 2013;950:171-93.
827   57.   Rosenthal PB, Henderson R. Optimal determination of particle orientation, absolute hand,
828   and contrast loss in single-particle electron cryomicroscopy. J Mol Biol. 2003;333(4):721-45.
829   58.   Pettersen EF, Goddard TD, Huang CC, Couch GS, Greenblatt DM, Meng EC, et al. UCSF
830   Chimera--a visualization system for exploratory research and analysis. J Comput Chem.
831   2004;25(13):1605-12.
832   59.   Emsley P, Lohkamp B, Scott WG, Cowtan K. Features and development of Coot. Acta
833   Crystallogr D Biol Crystallogr. 2010;66(Pt 4):486-501.
834   60.   Yang J, Zhang Y. I-TASSER server: new development for protein structure and function
835   predictions. Nucleic Acids Res. 2015;43(W1):W174-81.

836   61.   Phillips JC, Braun R, Wang W, Gumbart J, Tajkhorshid E, Villa E, et al. Scalable molecular
837   dynamics with NAMD. J Comput Chem. 2005;26(16):1781-802.
838   62.   Trabuco LG, Villa E, Mitra K, Frank J, Schulten K. Flexible fitting of atomic structures into
839   electron microscopy maps using molecular dynamics. Structure. 2008;16(5):673-83.
840   63.   Humphrey W, Dalke A, Schulten K. VMD: visual molecular dynamics. J Mol Graph.
841   1996;14(1):33-8, 27-8.
842   64.   Chen VB, Arendall WB, 3rd, Headd JJ, Keedy DA, Immormino RM, Kapral GJ, et al.
843   MolProbity: all-atom structure validation for macromolecular crystallography. Acta Crystallogr D
844   Biol Crystallogr. 2010;66(Pt 1):12-21.
845   65.   Jurrus E, Engel D, Star K, Monson K, Brandi J, Felberg LE, et al. Improvements to the
846   APBS biomolecular solvation software suite. Protein Sci. 2018;27(1):112-28.
847   66.   Pettersen EF, Goddard TD, Huang CC, Meng EC, Couch GS, Croll TI, et al. UCSF
848   ChimeraX: Structure visualization for researchers, educators, and developers. Protein Sci.
849   2021;30(1):70-82.
850   67.   Goddard TD, Huang CC, Meng EC, Pettersen EF, Couch GS, Morris JH, et al. UCSF
851   ChimeraX: Meeting modern challenges in visualization and analysis. Protein Sci. 2018;27(1):14-25.
852